A Tryptophan Neutral Radical in the Oxidized State of Versatile Peroxidase from *Pleurotus eryngii*
A COMBINED MULTIFREQUENCY EPR AND DENSITY FUNCTIONAL THEORY STUDY*

Rebecca Pogni[‡1], **M. Camilla Baratto**[‡], **Christian Teutloff**[§], **Stefania Giansanti**[‡], **Francisco J. Ruiz-Dueñas**[¶2], **Thomas Choinowski**[‖], **Klaus Piontek**[‖], **Angel T. Martínez**[¶], **Friedhelm Lendzian**[§3], and **Riccardo Basosi**[‡]

From the [‡]Department of Chemistry, University of Siena, 53100 Siena, Italy, the [§]Max Volmer Laboratory for Biophysical Chemistry, Technical University Berlin, D-10623 Berlin, Germany, the [¶]Centro de Investigaciones Biológicas, Consejo Superior de Investigaciones Científicas, E-28040 Madrid, Spain, and the [‖]Institute of Biochemistry, Swiss Federal Institute of Technology, CH-8093 Zürich, Switzerland

Versatile peroxidases are heme enzymes that combine catalytic properties of lignin peroxidases and manganese peroxidases, being able to oxidize Mn^{2+} as well as phenolic and non-phenolic aromatic compounds in the absence of mediators. The catalytic process (initiated by hydrogen peroxide) is the same as in classical peroxidases, with the involvement of 2 oxidizing equivalents and the formation of the so-called Compound I. This latter state contains an oxoferryl center and an organic cation radical that can be located on either the porphyrin ring or a protein residue. In this study, a radical intermediate in the reaction of versatile peroxidase from the ligninolytic fungus *Pleurotus eryngii* with H_2O_2 has been characterized by multifrequency (9.4 and 94 GHz) EPR and assigned to a tryptophan residue. Comparison of experimental data and density functional theory theoretical results strongly suggests the assignment to a tryptophan neutral radical, excluding the assignment to a tryptophan cation radical or a histidine radical. Based on the experimentally determined side chain orientation and comparison with a high resolution crystal structure, the tryptophan neutral radical can be assigned to Trp^{164} as the site involved in long-range electron transfer for aromatic substrate oxidation.

Different heme peroxidases are considered to be involved in the lignin biodegradation process, a key step for carbon recycling in terrestrial ecosystems. These are lignin peroxidase (LiP)[4] and manganese peroxidase (MnP), first described in *Phanerochaete chrysosporium* (1–3), and the versatile peroxidase (VP), more recently described in fungi from the genera *Pleurotus* (4–6) and *Bjerkandera* (7, 8). VP is characterized by combining catalytic properties of the other two ligninolytic peroxidases, MnP and LiP. This enzyme is able to oxidize Mn^{2+} to Mn^{3+} and also

exhibits manganese-independent activity toward veratryl alcohol and *p*-dimethoxybenzene. Furthermore, it oxidizes hydroquinones and substituted phenols that are not efficiently oxidized by LiP or MnP in the absence of veratryl alcohol and Mn^{2+}, respectively. VP is even able to degrade directly high redox potential dyes, which can be eventually oxidized by LiP only in the presence of veratryl alcohol (9, 10).

Two genes encoding VP isoenzymes VPL and VPS1, expressed in liquid- and solid-state fermentation cultures, respectively, have been cloned from *Pleurotus eryngii* (11, 12). The deduced amino acid sequences for both isoenzymes were used to build molecular models by homology modeling, taking advantage of sequence identity to *P. chrysosporium* LiP and MnP and *Coprinopsis cinerea* (synonym *Coprinus cinereus*) peroxidase (13). Very recently, the crystal structure of recombinant *P. eryngii* VP expressed in *Escherichia coli* and activated *in vitro* (14) has been determined at 1.33-Å resolution (Protein Data Bank code 2BOQ).

Catalytically, VP would follow the classical heme peroxidase cycle, in which hydrogen peroxide is the final electron acceptor, acting as a 2-electron oxidizing substrate for the resting enzyme, which results in the formation of Compound I (15–17). Compound I is reduced back by the substrate in a two-step reaction that involves the formation of Compound II (a 1-electron oxidized form) and then the closure of the catalytic cycle to the resting state. It is known that H_2O_2 attains the distal side of the heme through the access channel present in all peroxidases. However, identification of sites involved in substrate oxidation has been successful only on a few occasions (18–20).

In ligninolytic peroxidases, only the manganese interaction site in MnP, situated near the internal propionate of the heme, has been confirmed by site-directed mutagenesis and x-ray diffraction of MnP·Mn^{2+} complexes (21–23). A putative manganese-binding site similar to that of MnP has been identified in *P. eryngii* VP isoenzymes (12, 24). Substitution of one of the residues from the putative manganese interaction site in VPL yields an enzyme with its Mn^{2+} oxidation ability strongly impaired (25). Such a binding site is not present in LiP according to its lack of activity with this divalent cation.

In the case of LiP, there is no x-ray structure with any of its substrates available, and structure-function studies have been based on techniques that led to the indirect characterization of the substrate interaction sites. The veratryl alcohol molecule was initially modeled at the heme access channel (26), and the residues hypothetically involved are conserved also in the isoenzyme VPS1 of *P. eryngii*, which has a main heme access channel remarkably similar to that of LiP (24). Apart from the possibility of direct electron transfer to the heme from some substrates, long-range electron transfer (LRET) should be considered to justify the capacity of

[1] To whom correspondence may be addressed. Tel.: 39-0577-23-4258; Fax: 39-0577-23-4239; E-mail: pogni@unisi.it.
[2] Supported by a Consejo Superior de Investigaciones Científicas I3P contract.
[3] To whom correspondence may be addressed. Tel.: 49-30-314-22489; Fax: 49-30-314-21122; E-mail: f.lendzian@tu-berlin.de.
[4] The abbreviations used are: LiP, lignin peroxidase from *P. chrysosporium*; MnP, manganese peroxidase from *P. chrysosporium*; VP, versatile peroxidase; LRET, long-range electron transfer; ENDOR, electron nuclear double resonance; DFT, density functional theory; hf, hyperfine; VP*, recombinant versatile peroxidase; mT, milliteslas; mW, milliwatts.

VP and LiP to oxidize high molecular size substrates that do not fit into the heme access channel.

The first suggested LRET pathway involved the LiP distal histidine and started at His[82] (27). This pathway does not exist in MnP and in the isoenzyme VPL of *P. eryngii*, but it has been identified in VPS1. Two additional pathways have been proposed in LiP. One starts at the second exposed histidine (LiP His[239]) to the proximal histidine and is absent in MnP and VPS1 and present in VPL (His[232]). The second pathway starts from an exposed tryptophan (Trp[171]) present in LiP and proceeds to the porphyrin ring. Its involvement in veratryl alcohol and non-phenolic lignin model compound oxidation has been confirmed in LiP, and Trp[171] has been revealed to be a redox-active residue (28–32). Multisequence alignment revealed that the above-mentioned tryptophan residue is conserved in all LiP sequences as well as in *Pleurotus* VP and is absent in the typical MnP (15). The involvement of a surface tryptophan as a catalytic site in LiP was also inferred in a study on the S168W variant of MnP (33).

Moreover, a putative electron transfer pathway from the exposed tryptophan residue was identified in *P. eryngii* isoenzymes VPL (Trp[164]) and VPS1 (Trp[170]) (12, 13, 24). It is interesting to point out that VPs, as all other ligninolytic enzymes described until now, have no Tyr residues in their sequences (15).

In this work, we report the results from multifrequency (9.4 GHz, X-band; and 94 GHz, W-band) EPR studies on a freeze-quenched radical intermediate in the reaction of *P. eryngii* VP with H_2O_2. Comparison of the EPR and pulse electron nuclear double resonance (ENDOR) experimental data with theoretical results from density functional theory (DFT), in particular for the hyperfine (hf) tensor values, excludes assignment to a tryptophan cation radical or a histidine radical, but strongly suggests assignment to a tryptophan neutral radical. It has been shown in earlier studies on tryptophan radicals in ribonucleotide reductase variants that evaluation of the hf-tensors of the side chain methylene protons enables determination of the side chain geometry, which can be used for site-specific assignment (34, 35). Based on the side chain orientation deduced from the experimental hyperfine data of these protons, the observed tryptophan neutral radical can be assigned to Trp[164], which is proposed as the surface site involved in LRET in VPL of *P. eryngii*.

MATERIALS AND METHODS

Chemicals and Protein Preparation—Potassium hydrogen phthalate and H_2O_2 were purchased from Sigma and used without further purification. Recombinant VP (VP*) was obtained by *E. coli* expression (14), and the cDNA encoding the mature sequence of *P. eryngii* allelic variant VPL2 (GenBank[TM] accession number AF007222) (12) was cloned in the expression vector pFLAG1 and used to transform *E. coli* W3110. Transformed cells were grown for 3 h in Terrific Broth (36), induced with 1 mM isopropyl β-D-thiogalactopyranoside, and grown for an additional 4 h. The apoenzyme accumulated in inclusion bodies was recovered using 8 M urea. Subsequent *in vitro* folding was performed using 0.15 M urea, 5 mM Ca^{2+}, 20 μM hemin, oxidized glutathione/dithiothreitol (5:1), and 0.1 mg/ml protein at pH 9.5 (14). Active enzyme was purified by Mono Q chromatography using a 0–0.5 M NaCl gradient in 10 mM sodium tartrate (pH 5.5) supplemented with 1 mM $CaCl_2$.

UV-visible and EPR Measurements—UV-visible measurements of 6 μM VP* in 0.1 M phthalate buffer (pH 4.5) were performed on a Hewlett-Packard 8453 spectrophotometer at 24 °C before and after the addition of 8 eq of H_2O_2. EPR solutions were prepared with a final concentration of 0.16 mM enzyme and 1.3 mM H_2O_2 in the same buffer, and the reaction was stopped by rapid immersion of the EPR tube in liquid nitrogen after 10 s.

Continuous wave X-band (9.4 GHz) EPR measurements were carried out with a Bruker eleXsys E500 series using the Bruker ER4122 SHQE cavity and an Oxford ESR900 helium continuous flow cryostat. X-band pulse ENDOR experiments were performed on a Bruker E580 pulse EPR/ENDOR spectrometer using a Bruker EN4118X-MD4-W1 resonator equipped with a helium immersion cryostat. Spin quantification was performed by double integration of the experimental EPR radical signal compared with the iron signal.

EPR saturation data were collected by measuring the EPR absorption derivative signal intensity as a function of microwave power at different temperatures. The saturation data were fit to Equation 1,

$$S/\sqrt{P} = 1/(1 + (P/P_{1/2}))^{b/2} \qquad \text{(Eq. 1)}$$

where S is the EPR derivative signal intensity, P is the microwave power, $P_{1/2}$ is the half-saturation power, and b is the inhomogeneity parameter. A nonlinear least-squares fit to Equation 1 yielded $P_{1/2}$ and b values for each particular temperature (37–39).

94 GHz high-field EPR experiments were performed on a Bruker eleXsys E680 spectrometer. Spectra were recorded at 40 K. Low microwave power, typically only a few microwatts, was used to avoid saturation effects. For determination of precise g-tensor components, the microwave frequency was measured using a frequency counter, which was integrated in the spectrometer. The magnetic field was calibrated with a g-tensor standard (lithium in LiF, g = 2.002293 (2)) (40) at two different frequencies (typically, 93.8 and 94.2 GHz). All spectra were recorded in the "persistent mode" of the superconducting magnet, using the room temperature coils for the field sweep to ensure high linearity and stability of the field (maximum sweep width of 800 G). The modulation amplitude was kept at 0.2 millitesla (mT) to avoid modulation broadening. The 94 GHz EPR microwave resonator is a fundamental mode cylindrical cavity that has a high filling factor (compared with a transmission line set up or a Fabry-Perot resonator) and a small sample volume (0.7-mm diameter and ~1.5-mm height), thereby assuring high sensitivity and high homogeneity of the field over the active sample volume (>5 ppm). This enables the measurement of very accurate g-tensor values with an instrumental limit for the absolute g-tensor resolution obtained for the narrow signal of the g-tensor standard of $\pm$0.000005 (lithium in LiF, approximate line width of 0.01 mT).

Simulation of the EPR Spectra—The EPR spectra were analyzed using a software for simulating and fitting EPR spectra for $S = 1/2$ systems with anisotropic g- and hf-tensors (34). Thereby, the spectra are simulated by computing the resonant field position correct to second order at the given microwave frequency, dependent on the orientation of the g- and hf-tensors with respect to the external magnetic field (41, 42). No restriction for the relative orientation of the principal axes of the different tensors is applied (34).

DFT Calculations—DFT calculations were performed with the program package Gaussian 03 (43) at the unrestricted Kohn-Sham level using the hybrid exchange-correlation functional B3LYP. Geometry optimizations were done using a contracted basis set augmented with polarization functions (6–31G**) (43). Magnetic properties (g-tensor, spin densities, and hyperfine couplings) were calculated on the geometry-optimized structure in a second step using the TZVP basis set, which is included in the program. The resulting output was fed into the program MOLDEN for visualization of the spin density distribution in the molecule (44).
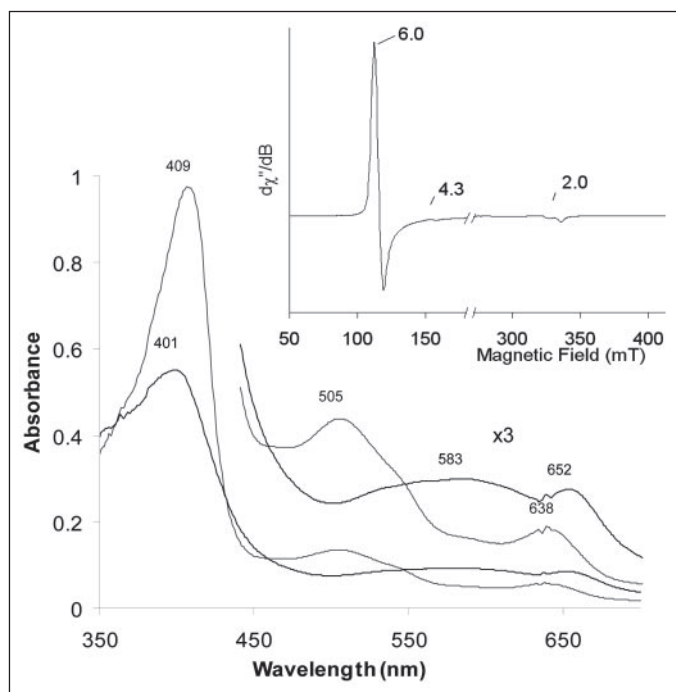
FIGURE 1. **Electronic absorption spectra of *P. eryngii* VP* at resting state (*gray lines*) and Compound I (*black lines*) at 24 °C in 0.1 M phthalate buffer (pH 4.5).** VP* was measured after a 10-s reaction with 8 eq of H_2O_2. The region between 450 and 700 nm has been expanded 3-fold. *Inset*, X-band EPR spectra of resting *P. eryngii* VP* (Fe(III) spin state before the addition of H_2O_2). The spectrum was recorded under the following conditions: temperature, 20 K; $\nu = 9.385$ GHz; modulation amplitude, 1 mT; microwave power, 2 mW; and modulation frequency, 100 kHz.

RESULTS

UV-visible Spectroscopy—Fig. 1 shows the electronic absorption spectrum of *P. eryngii* VP* (expressed in *E. coli* and folded *in vitro*) at pH 4.5 before and after H_2O_2 addition. The spectrum is characterized by the presence of the Soret band at 409 nm and the two charge transfer bands at 505 and 638 nm. The 600–650-nm wavelength region is sensitive to the heme pocket environment (45). This band (638 nm), observed only in the high spin state, has been assigned to a charge transfer transition from the porphyrin to the iron. In the *inset* of Fig. 1, the EPR spectrum of the resting state enzyme confirms the presence of the dominant contribution of the high spin iron species ($g_\perp = 6.00$ and $g_\parallel = 2.00$).

In the UV-visible spectrum (Fig. 1) recorded 10 s after the addition of 8 eq of H_2O_2, the Soret absorption band is broadened, and its intensity is reduced with respect to the native enzyme. The visible region shows a broad absorption with peaks at 583 and 652 nm, suggesting the formation of Compound I (17, 46).

The reduced absorption of the Soret region of Compound I compared with native VP* and the characteristic absorption band at 652 nm suggest that this compound contains 2 oxidizing eq over the native enzyme (47). The first oxidizing equivalent is contained in the ferryl state of the iron. The second equivalent can be on the porphyrin ring, as for horseradish peroxidase, or on an amino acid side chain of the protein, as for cytochrome *c* peroxidase (16, 17). Through EPR measurements, it is possible to distinguish the oxidizing equivalent location and to assign the nature of the organic radical formed.

9.4 GHz EPR Spectroscopy—In Fig. 2, the EPR signal obtained after the addition of 8 eq of H_2O_2 and rapid cooling is shown. The strong decrease in the EPR signal of the ferric high spin species and the formation of an intense radical signal corresponding to a protein radical species are evident. The yield of the radical signal is ~0.25 spin/heme.
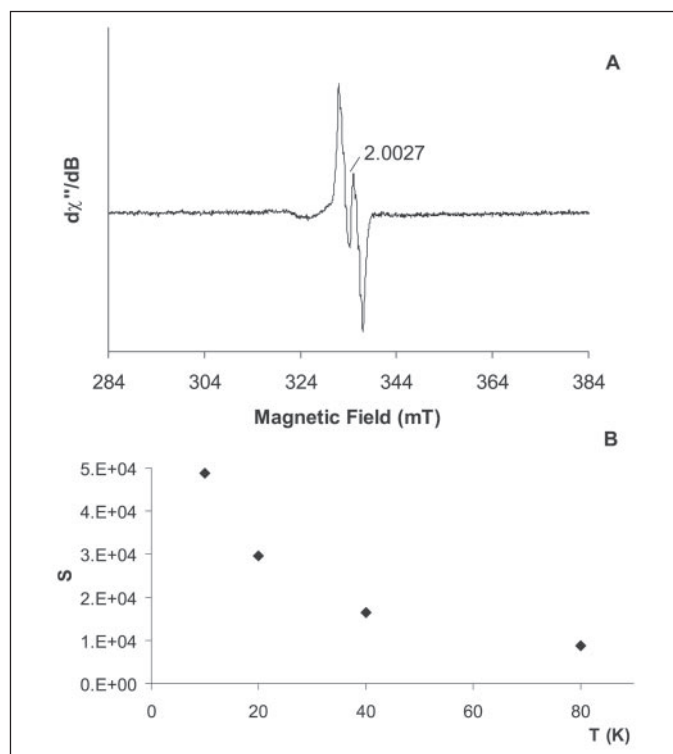

FIGURE 2. *A*, low temperature (20 K) EPR spectrum of the enzyme radical obtained 10 s after the addition of H_2O_2. The spectrum was recorded under the following conditions: $\nu = 9.385$ GHz; modulation amplitude, 0.2 mT; microwave power, 2 mW; and modulation frequency, 100 kHz. *B*, effect of increasing temperature on the signal intensity.
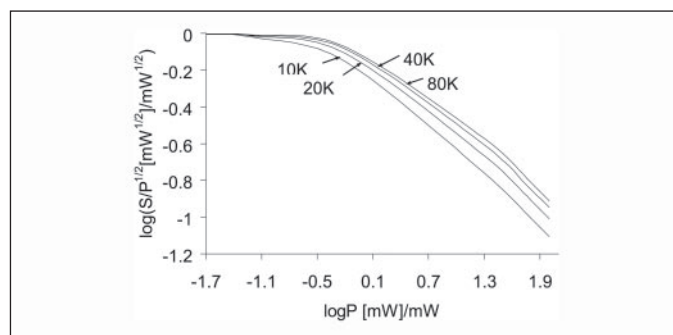

FIGURE 3. **Continuous microwave power saturation curves for the radical signal at g = 2.0027 recorded at 10, 20, 40, and 80 K.** The $\log(S/\sqrt{P})$ ($mW^{1/2}/mW^{1/2}$), where *S* is the area of the normalized derivative signal and *P* is the microwave power, *versus* log P (mW/mW) is reported. EPR spectra were recorded under the following conditions: $\nu = 9.386$ GHz; modulation amplitude, 0.2 mT; modulation frequency, 100 kHz; and microwave powers, 0.02, 0.06, 0.63, 20, 63, and 100 mW.

The isotropic EPR spectrum shown in Fig. 2*A* is characterized by a doublet, centered at g = 2.0027. It seems that the reaction of the heme porphyrin ring and H_2O_2 proceeds to the formation of an amino acid radical, considering the absence of the characteristic signal of the ferryl porphyrin intermediate at 10 s of freezing time (48, 49). In Fig. 2*B*, the intensity of the radical signal against temperature is plotted. The curve shows a strong temperature dependence especially at low temperature, as reported for cytochrome *c* (50).

Fig. 3 represents $\log(S/\sqrt{P})$ ($[mW^{1/2}]/mW^{1/2}$) against log *P* ([mW]/mW), and the values of $P_{1/2}$ and *b* (Equation 1) can be calculated for all different temperatures. At 20 K, the *b* value obtained from the fitting is equal to 0.9. This is typical for protein radicals with a weak coupling to a paramagnetic ion. The $P_{1/2}$ value is in good agreement with those
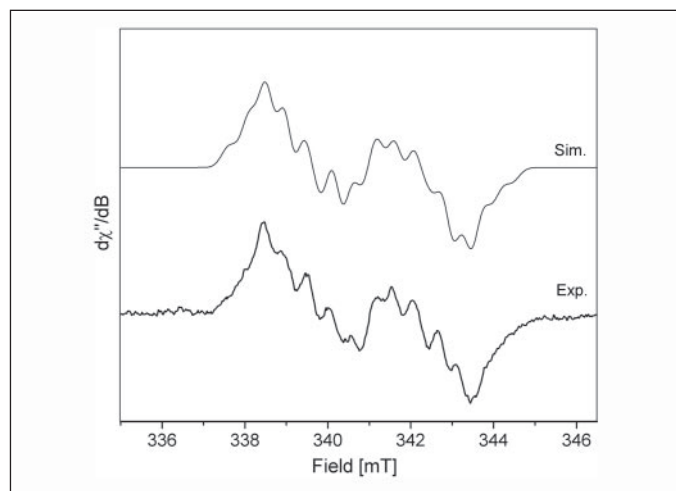
FIGURE 4. **High resolution narrow scan 9.5 GHz EPR spectrum of the radical reported in Fig. 2 together with the best simulation (see "Results").** EPR spectra were recorded under the following conditions: microwave power, 0.5 mW; modulation amplitude, 0.1 mT; and temperature, 40 K. Parameters for the EPR simulation (*Sim.*) are given in Table 1. *Exp.*, experimental.

reported for similar organic radicals that coupled to the ferryl heme iron in other peroxidase systems (51, 52).

An expansion of the well resolved 9.4 GHz (X-band) EPR spectrum of the radical is shown in Fig. 4. The spectrum is dominated by a large doublet splitting, showing well resolved subsplittings on each of the two components. The overall shape of the spectrum is very symmetric, which is expected in the case of very small g-tensor anisotropy. The *upper trace* shows a best simulation and fit of the spectrum based on one nitrogen and two anisotropic ring proton hf-tensors, typical for a tryptophan radical (34, 52, 53), and two fairly isotropic hf-tensors from the β-protons of the side chain. The simulation shows that the 9.5 GHz EPR spectrum is fully consistent with the proton and nitrogen hf-tensor values, typical for a tryptophan neutral radical (Scheme 1). The g-tensor values obtained from the 94 GHz EPR spectrum were used in the simulation shown in Fig. 4 (see below and Table 1). At 9.5 GHz, the EPR simulation is very sensitive for the hf-tensor values, but less sensitive for the g-tensor values in the case of such small g-tensor anisotropy. The obtained hf-tensor values are given in Table 1.

High-field EPR Spectroscopy (94 GHz Frequency)—To unequivocally identify the nature of the observed radical, we performed high-field/high frequency EPR experiments on samples of *P. eryngii* VP*, prepared in the same way as those used for recording the 9.4 GHz EPR spectra. Although the hyperfine structure observed in conventional X-band EPR can be rather similar for different types of organic radicals, it has been demonstrated that the principal values ($g_{xx,yy,zz}$) of the g-tensor, which are resolved for such radicals only in high-field EPR, can serve as a molecular fingerprint for identification of the type of radical (48, 49, 51–53). In particular, tyrosine and tryptophan radicals are difficult to distinguish in X-band (9.4 GHz) EPR, whereas at 94 GHz EPR, they are clearly distinguished based on the much larger g_{xx} and g_{yy} values observed for tyrosyl radicals exhibiting large spin density on the oxygen, which has a large spin orbit coupling constant, compared with tryptophan radicals with spin density only on carbons and nitrogen, both being nuclei with only small spin orbit coupling constants (51–53). For a tryptophan radical, the field corresponding to 94 GHz EPR (3.3 tesla) does still not represent the so-called high-field limit, where the g-tensor shifts exceed the hyperfine splitting and all three g-tensor components are separated in the spectrum. This situation was nearly met at 285 GHz EPR in a study of a tryptophan radical in azurin (54). However, the
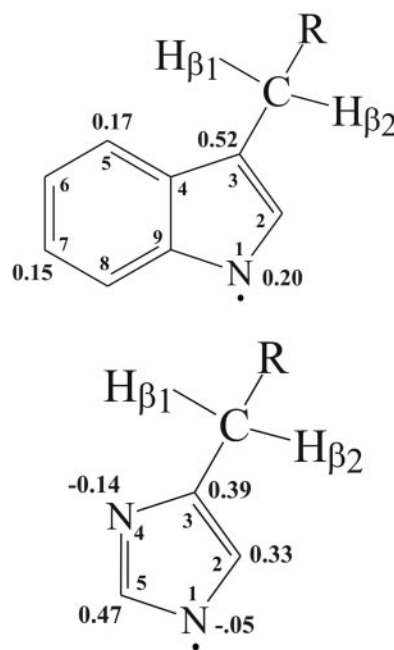
SCHEME 1. **Molecular structures of the tryptophan (*upper*) and histidine (*lower*) neutral radicals.** The *inner numbers* denote the molecular positions, which were chosen for the histidine radical so as to have the same numbering for comparable positions, except for positions 5 (His) and 9 (Trp). The *outer numbers* are π-spin densities derived from the experimental hf-tensors (see "Discussion").

hf-tensor resolution in the spectrum was lost at 285 GHz. Nevertheless, at 94 GHz EPR, the g-tensor anisotropy contributes already significantly to the shape and overall width of the spectrum, and the g-tensor values can be obtained from EPR simulations, provided partially resolved hyperfine splitting is observed at 94 GHz, and all hf-tensor values are known from 9.5 GHz EPR experiments (53).

Fig. 5 shows the 94 GHz high-field EPR spectrum from the radical obtained at 40 K. The spectrum is again dominated by a large doublet splitting. However, different from the X-band EPR spectrum, it shows a clear asymmetry; the low-field side shows a sharper rise and is more structured, whereas the high-field side has a more extending wing with weak intensity. This asymmetry in the spectrum is indicative of the presence of small g-tensor anisotropy, which nevertheless significantly affects the 94 GHz EPR spectrum.

The *upper trace* in Fig. 5 shows a best simulation and fit of the spectrum, from which the g- and hf-tensor values were obtained. 94 GHz EPR simulations were started using the proton and nitrogen hf-tensor values from the X-band EPR simulations. The simulated 94 GHz EPR spectrum is particularly sensitive to the g-tensor values. The spectral positions of the g_{xx}, g_{yy}, and g_{zz} components shown in Fig. 5 indicate the magnitude of the g-tensor anisotropy, which significantly determines the overall width, shape, and splitting of the simulated 94 GHz spectrum. The X-band EPR spectrum of the radical was then simulated using the g-tensor values from the 94 GHz EPR simulations, in this way refining the hf-tensor values.

The final simulations shown in Figs. 4 and 5 were performed for the 9.4 and 94 GHz EPR spectra using the same g- and refined hf-tensor values (Table 1), which fitted both spectra equally well. We want to emphasize that only this multifrequency approach ensures obtaining a unique set of g- and hf-tensor values for the radical. Table 1 shows that the g- and hf-tensor values for the radical in *P. eryngii* VP* agree very well with values recently obtained for a tryptophan neutral radical in

TABLE 1

g- and hf-tensor principal components for the tryptophan radical in *P. eryngii* VP* in comparison with the tryptophan radicals in *B. adusta* VP (52) and the Y122F variant of *E. coli* ribonucleotide reductase (34)

Radical	g_i [a]	A_{iso}(H-β1)	A_{iso}(H-β2)	A_{iso}(H-5)	A_{iso}(H-7)	A_{iso}(N)	A_{iso}(H-2)	A_{iso}(N . . . H-OH)
		mT [b,c]	mT [b,c]	mT [b,c]	mT [b,c]	mT [b,d]	mT [b]	mT [e]
***P. eryngii* VP (this work)**								
xx	2.00352	2.35	1.13	-0.64	$\leq\lvert0.15\rvert$	$\leq\lvert0.15\rvert$	0.28 [f]	-0.10 [e]
yy	2.00255	2.75	1.13	$\leq\lvert0.15\rvert$	-0.62	$\leq\lvert0.15\rvert$	-0.04 [f]	0.19 [e]
zz	2.00220	2.70	1.18	-0.49	-0.46	1.00	-0.11 [f]	-0.07 [e]
***B. adusta* VP (52)**								
xx	2.0035	2.15	1.75	-0.64	$\leq\lvert0.15\rvert$	$\leq\lvert0.15\rvert$	ND [g]	ND
yy	2.0025	2.30	1.95	$\leq\lvert0.15\rvert$	-0.62	$\leq\lvert0.15\rvert$	ND	ND
zz	2.0022	2.30	1.95	-0.49	-0.46	1.05	ND	ND
Trp[111]·/Y122F of *E. coli* RNR (34, 53)								
xx	2.0033	2.70	1.38	-0.68	$\leq\lvert0.1\rvert$	$\leq\lvert0.15\rvert$	ND	-0.10 [e]
yy	2.0024	2.75	1.38	$\leq\lvert0.1\rvert$	-0.61	$\leq\lvert0.15\rvert$	ND	0.19 [e]
zz	2.0022	2.83	1.38	-0.50	-0.51	1.05	ND	-0.07 [e]
DFT [h]								
Trp neutral radical (21° to plane)								
xx	2.00372	2.73	1.07	-0.60	-0.10	-0.13	0.17	-0.08
yy	2.00291	3.06	1.12	-0.18	-0.56	-0.12	-0.03	0.18
zz	2.00248	2.79	1.38	-0.47	-0.37	1.19	-0.13	-0.06
Trp neutral radical (85° to plane)								
xx	2.00369	0.76	0.41	-0.64	-0.12	-0.12	0.16	-0.08
yy	2.00283	1.10	0.44	-0.18	-0.61	-0.11	-0.07	0.17
zz	2.00245	0.78	0.70	-0.50	-0.40	1.11	-0.15	-0.06

[a] The g-tensor principal values ($g_{xx,yy,zz}$) are given with a maximum error of ±0.0001. The g_z axis is expected to be out of the tryptophan plane (34, 53, 62); the g_x axis is in the tryptophan plane and forms an angle of ~20° with the line connecting the center of the C-6–C-7 bond with C-2 (Scheme 1).

[b] hf-tensor principal components are given in mT (estimated error of ±0.05 mT). The g- and hf-tensor values fit X- and W-band EPR spectra equally well (Figs. 4 and 5). The remaining deviations are small and could be a result of weak coupling to the Fe^{4+} ion ($S = 1$ ground state) of the heme. g-tensor and ring proton hf-tensor values (in mT) are similar to those obtained recently from the tryptophan neutral radical in *B. adusta* (52) and previously reported for the Y122F variant of *E. coli* RNR (34, 53) (see center rows). The differences in the hf-tensor values of the side chain protons H-β1 and H-β2 do not reflect different spin densities at C-3 (Scheme 1), but rather result from different dihedral angles for different side chain orientations (see "Discussion").

[c] Negative signs are for ring proton hf-tensor values expected from theory in the case of positive carbon spin density; for the simulations, the *x* axes of H-5 and H-7 hf-tensors were rotated 30° with respect to the g-tensor *x* axis (estimated error of ±0.05 mT).

[d] The axis of A_{zz}(N-1) is parallel to the g_z axis, as expected for a nitrogen in a planar π-system (34, 53).

[e] The hf-tensor was assigned to the proton of a hydrogen bond donor to the indole nitrogen of the tryptophan neutral radical (Fig. 7A).

[f] Small hf-tensor components are for H-2 (Scheme 1) and for the proton hydrogen-bonded to N-1 from the ENDOR spectra and their simulations (Fig. 6). Principal axes are not related to g-tensor axes.

[g] ND, not determined.

[h] Theoretical g- and hf-tensor principal values are from DFT for the tryptophan neutral radical, hydrogen-bonded at N-1 to a water molecule (Fig. 7) using Gaussian 3.0 (B3LYP, TZVP basis set) (43). A comparison of calculated g- and hf-tensor values for the tryptophan neutral and cation radicals using, in addition, the EPRII basis set, yielded the same values within ~5% for the larger tensors. Side chain orientation 85° out of plane corresponds to dihedral angles of ~55° and ~65° for H-β1 and H-β2 (orientation for Trp[244]) (Fig. 9). Side chain orientation 21° out of plane corresponds to dihedral angles of −9° for H-β1 and 52° for H-β2 (crystal structure for Trp[164]) (Figs. 7 and 9 and Table 2). The experimental values are in agreement only with an assignment to Trp[164] (see "Discussion").

Bjerkandera adusta VP (52), as well as with an earlier study on the Y122F variant of the ribonucleotide reductase from *E. coli* (34, 53).

9.5 GHz ENDOR Spectroscopy—Smaller couplings, *e.g.* from positions of small or negative spin densities in the indole ring or from a proton hydrogen-bonded to the nitrogen in a tryptophan neutral radical, are not resolved in the EPR spectra. They are resolved, however, by ENDOR spectroscopy. This technique gives basically the NMR spectrum of the respective radical detected via the electron (55). ENDOR lines from protons (hydrogens) occur as pairs in the spectra according to the first-order resonance condition (Equation 2),

$$\nu_{ENDOR} = \lvert \nu_H \pm A_j/2 \rvert \qquad \text{(Eq. 2)}$$

where ν_H represents the Larmor frequency of the proton ($I = 1/2$, $\nu_H = 14.9$ MHz at a magnetic field of 345 mT) and A_j ($j = xx, yy, zz$) is the electron-nuclear hyperfine coupling. In frozen solution, the hyperfine coupling is anisotropic, defined by three tensor principal components, $A_{xx}, A_{yy},$ and A_{zz} (55). According to Equation 2, each proton gives rise to a group of three pairs of spectral features (one pair for each component $A_{xx,yy,zz}$) that are spaced symmetrically about ν_H or $A_j/2$, whichever value is larger.

Fig. 6 shows a Davies pulse ENDOR spectrum (56) from the radical in *P. eryngii* VP*. Because of the low radical yield for the freeze-quenched reaction of VP* with H_2O_2 and unfavorable spin relaxation rates, probably caused by the nearby Fe^{4+}=O heme ($S = 1$), the ENDOR spectrum shows noise, even after ~7 h of accumulation. Therefore, we concentrated on the range of smaller hyperfine couplings, which give larger ENDOR signal intensities and are not resolved in the EPR spectra. Several pairs of lines are clearly detected in Fig. 6 and are spaced symmetrically about the free proton Larmour frequency ($\nu_H = 14.9$ MHz). The broad line groups at 7–10 and 20–24 MHz result from the two larger tensor components of protons 5 and 7 of the indole ring (Scheme 1). The *lower trace* in Fig. 6 shows a simulation of the ENDOR spectrum in the experimental frequency range using the hf-tensor components determined by EPR (Table 1). The extra intensity on the high frequency side (20–24 MHz) results from superposition of the low frequency lines (Equation 2) from the large β-proton hf-tensor values (H-β1). The low frequency lines from the smaller β-proton hf-tensor values (H-β2) are expected to be close to zero frequency, where intensities decrease strongly beyond detection. The respective high frequency lines of H-β1 and H-β2 are expected at frequencies ≥30 MHz, beyond the spectral range analyzed. Both hf-tensors from these protons are well resolved, however, in the EPR spectra and were analyzed.

Smaller hyperfine couplings (not resolved in the EPR spectra) give rise to the ENDOR line pairs between 11 and 18 MHz. Lines are observed corresponding to hf-tensor components of 0.28, 0.19, and ~0.11 mT and a smaller component between 0.07 and 0.04 mT with larger intensity, probably indicating contributions from two protons (0.1 mT obtained from the EPR spectra corresponds to 2.8 MHz
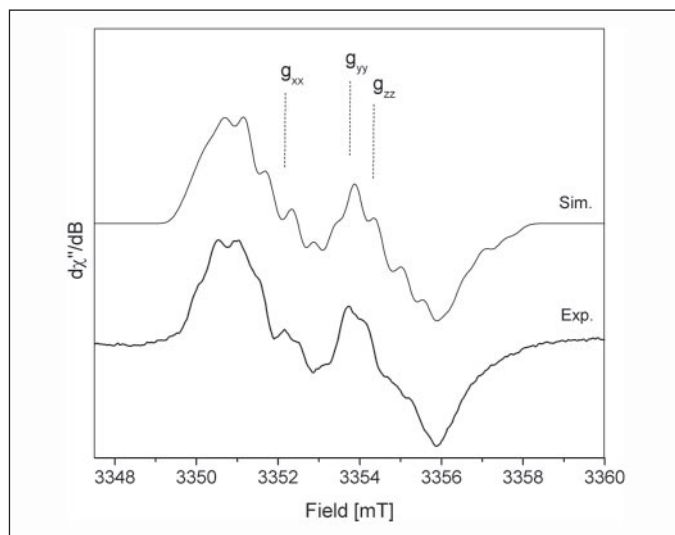
FIGURE 5. **94 GHz EPR spectrum of the protein radical together with the best simulation.** EPR spectra were recorded under the following conditions: microwave power, 0.25 microwatts; modulation amplitude, 0.2 mT; and temperature, 40 K. The positions for the three g-tensor principal values are shown to indicate the significant contribution of g-tensor anisotropy in the spectrum. The shape of the 94 GHz EPR spectrum is clearly asymmetric, and its total width is increased compared with that of the spectrum at 9.5 GHz due to the larger shifts of the g-tensor components at the correspondingly higher field (3.3 versus 0.34 teslas). The g- and hf-tensor components used for the simulation (*Sim.*) are the same as in Fig. 4 (Table 1), except for a somewhat larger intrinsic line width (0.4 versus 0.35 mT for the 9.5 GHz EPR spectrum). *Exp.*, experimental.
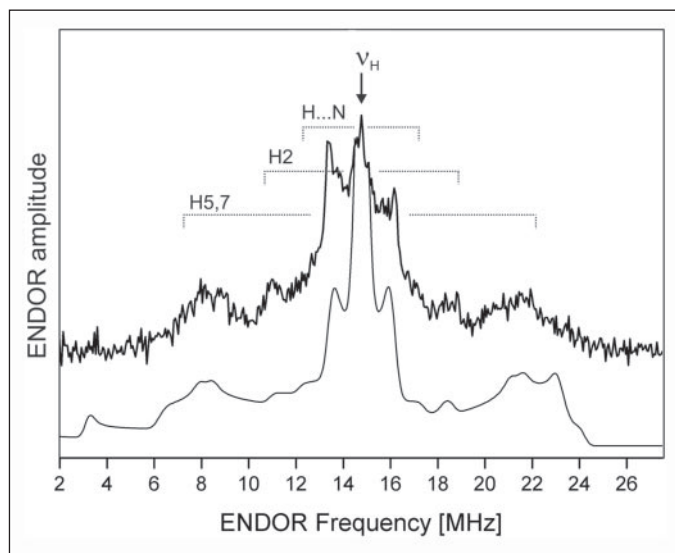

FIGURE 6. **Davies pulse ENDOR spectrum (56) of the radical in *P. eryngii* VP*.** Experimental parameters were as follows: temperature, 20 K; microwave pulse durations, 64 ns ($\pi/2$-pulse) and 112 ns (π-pulse); radio frequency (NMR) pulse duration, 5 μs; number of scans, 300; and total accumulation time, ~7 h. ENDOR line pairs are spaced symmetrically around ν_H (14.9 MHz). The *lower trace* is a simulation of the ENDOR spectrum, where the larger hf-tensor values (from H-5, H-7, H-β1, and H-β2) were taken from Table 1. The extra intensity at 23 MHz results from the low frequency transition of the β-proton H-β2. Both high frequency transitions of H-β1 and H-β2 are beyond 30 MHz (see "Results"). The molecular assignment of the lines is indicated (Scheme 1).

obtained from the ENDOR spectra). The best ENDOR simulation (Fig. 6) was obtained assuming two proton hf-tensors with the principal values given in Table 1 (last two columns). Comparison with the results from the DFT calculations (see below) shows that these couplings can be assigned to the hydrogen at C-2 (Scheme 1) and to a proton from a hydrogen bond to N-1 in the case of a tryptophan neutral radical (Fig. 7, Table 1, columns 7 and 8, and Table 2, row 2).

The presence of these two small anisotropic proton hf-tensors

strongly supports an assignment to a tryptophan neutral radical, hydrogen-bonded at N-1. In the tryptophan cation radical, a hydrogen forms a real covalent bond to N-1. In this case, an additional large hf-tensor, larger as for position 5, was calculated (data not shown), which is in disagreement with the experimental value (see "Discussion").

DFT Calculations—To corroborate the assignment of experimental hf- and g-tensor components and to further investigate the question of the presence of a tryptophan neutral or cation radical (both forms were observed in DNA photolyase) (57), we performed density functional calculations of spin densities and hf- and g-tensors (43, 44). Earlier DFT studies on tryptophan radicals were reported with qualitatively similar results for the hf-tensors (34, 58). However, we performed our own DFT calculations with the program package Gaussian 03 (43) at the restricted Kohn-Sham level using the hybrid exchange-correlation functional B3LYP and a TZVP basis set, in particular for the correct side chain geometry obtained from the x-ray structure, to obtain the g-tensor and taking into account hydrogen bonding by introducing water molecules. Inspection of the structure of tryptophans in various proteins shows a large variety of side chain geometries. It seems obvious that the actual side chain orientation is largely imposed by constraints of the protein and not by a small energy minimum of the isolated tryptophan molecule. After performing a general geometry optimization, we performed calculations for the tryptophan neutral radical with two fixed side chain orientations: (i) 85° out of plane, which corresponds approximately to Trp[244] in the crystal structure of *P. eryngii* VP, and (ii) only 21° out of plane, which corresponds to the side chain orientation of Trp[164] in VP. The best agreement with experimental hf-tensor values was obtained for the tryptophan neutral radical, deprotonated and hydrogen-bonded at N-1. For the above two side chain orientations of this radical, all calculated larger hf-tensor and g-tensor components are listed in Table 1 and compared with the experimental values.

Table 2 compares experimental π-spin densities derived from the measured hf-tensors with theoretical Mulliken spin densities (43, 44), calculated by DFT for a tryptophan cation and neutral radical. The experimental π-spin density for N-1, $\rho^\pi(^{14}N\text{-}1)$, was estimated from the anisotropic $^{14}N_1$ hf-tensor with elements $A'_{ii} = A_{ii} - A_{iso}$ ($ii = xx, yy, zz$), where $A_{iso} = (A_{xx} + A_{yy} + A_{zz})/3$. Assuming axial symmetry ($A'_{xx} = A'_{yy}$), the magnitude of this tensor is determined by the uniaxial constant B (59), where $A'_{zz} = 2B\rho^\pi(^{14}N\text{-}1)$ and $A'_{xx} = A'_{yy} = -B\rho^\pi(^{14}N\text{-}1)$. Using the $^{14}N_1$ hf-tensor values from Table 1 and the value of $B = 47.8$ MHz (1.706 mT) given for $\rho^\pi(^{14}N\text{-}1) = 1$ (59), an experimental π-spin density of $\rho^\pi(^{14}N\text{-}1) = 0.20$ was obtained (34, 53). For the α-protons at ring positions 5 and 7, π-spin densities were estimated from the hf-tensor elements of the respective protons (Table 1) using the relation $A_{iso}(H_\alpha) = Q\rho^\pi(C\text{-}5/7)$, with an established Q value of -2.48 mT (60). The π-spin density at C-3 was obtained from the hf-tensors of the two side chain β-protons H-β1 and H-β2 as discussed below. Calculated Mulliken spin densities are given in Table 2 for the tryptophan neutral radical, deprotonated and hydrogen-bonded at N-1 to a water molecule for the two side chain conformations (85° and 21° out of plane); for the tryptophan cation radical, with a N–H bond at N-1; and for the respective neutral and cation radicals of histidine. A visualization of the calculated Mulliken spin densities is given in Figs. 7 and 8.

DISCUSSION

The VP Radical Is a Tryptophan Neutral Radical—Identification and assignment of radicals immobilized in proteins are not straightforward, and simulations of conventional 9.4 GHz EPR spectra alone may lead to ambiguities, *viz.* that more than one set of g- and hf-tensor data may fit the observed EPR spectrum equally well. However, the multifrequency

FIGURE 7. **Spin densities calculated with DFT (43), visualized using a contour value of 0.005 with the program MOLDEN (44).** The molecular structure was energy-minimized, including the water molecule hydrogen-bonded at N-1. *A*, tryptophan neutral radical, hydrogen-bonded to a water molecule at N-1 (for numbering, see Scheme 1), with a side chain orientation 21° out of plane, corresponding to the geometry of Trp[164] in the crystal structure (see Fig. 9). *B*, tryptophan cation radical, with an N-1–H covalent bond. *Blue*, positive spin densities; *red*, negative spin densities. Note that the cation radical has reduced spin densities at C-3 (where the side chain is attached) and at N-1 and additional large spin density between these two positions at C-2. The larger spin densities for both molecules are given in Table 2. The experimental results agree only for the neutral radical (*A*; see "Results").
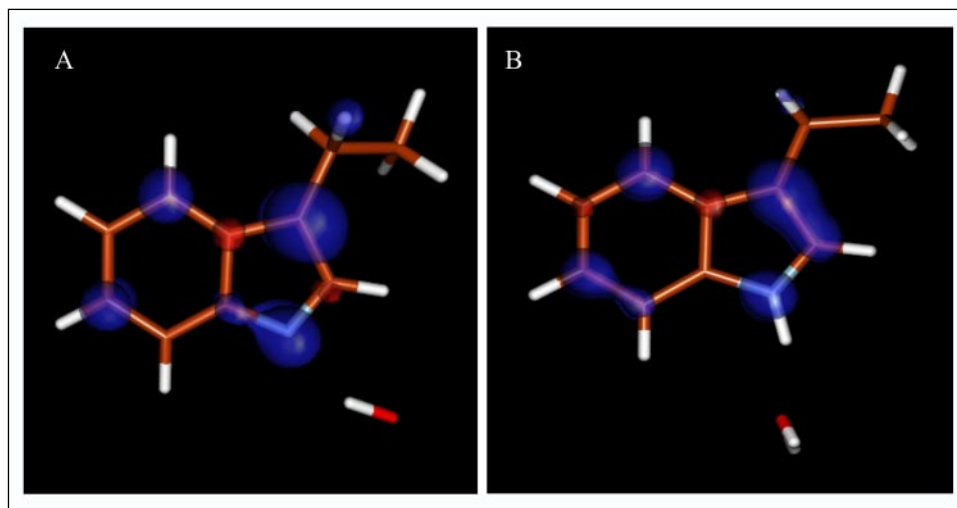

TABLE 2

π -Spin densities derived from experimental hf- and g-tensors for the tryptophan radical in *P. eryngii* VP* in comparison with theoretical spin densities and g-tensors calculated by DFT for tryptophan and histidine neutral and cation radicals

Molecular position (Scheme 1)	*P. eryngii* (this work)[a]	Trp neutral radical (85° to plane)[b]	Trp neutral radical (21° to plane)[b]	Trp cation radical[b,c]	His neutral radical (in plane)[b,d]	His cation radical[b,d]
N-1	0.20	0.26	0.28	0.16	−0.05	−0.10
C-2	≤|0.05|	−0.09	−0.10	0.13	0.33	0.33
C-3	0.52	0.61	0.61	0.44	0.39	0.40
N-4 (His)	NA[e]	NA	NA	NA	−0.14	−0.11
C-5	0.17	0.23	0.22	0.26	0.47	0.46
C-7 (Trp)	0.15	0.18	0.16	0.17	NA	NA
g_{xx}	2.00352	2.00369	2.00372	2.00344	2.00295	2.00290
g_{yy}	2.00255	2.00283	2.00291	2.00249	2.00187	2.00199
g_{zz}	2.00220	2.00245	2.00245	2.00253	2.00235	2.00232

[a] π-Spin densities (ρ^{π}) at C-3, C-5, and C-7 were estimated from the experimental hf-tensor values (see "Results"). Isotropic hyperfine coupling values, $A_{\mathrm{iso}} = (A_{xx} + A_{yy} + A_{zz})/3$, from both H-$\beta$1 and H-$\beta$2 were used for estimating ρ^{π} (C-3) (see "Results").

[b] DFT calculations were made with the program Gaussian 03 (43) using the B3LYP functional and the TZVP basis set for final calculation of the spin densities and g- and hf-tensors of the respective radical (see "Results"). Given are the Mulliken atomic spin densities (ρ^{π}) for all molecular positions where $\rho^{\pi} > |0.06|$. The orientation of the side chain with respect to the tryptophan head group was changed and found to have no major influence on the spin densities within the indole ring system. However, the hf-tensor values of the side chain β-protons strongly depend on the side chain orientation (see Eq. 3 and "Discussion"). The 21° out-of-plane orientation of the side chain corresponds to the geometry of Trp[164] in the crystal structure of *P. eryngii* VP and is close to the orientation deduced from the experimental values of the β-proton hf-tensors. The 85° out-of-plane orientation corresponds to Trp[244] and does not agree with the experiments (see Fig. 9 and "Discussion"). The tryptophan neutral radical is deprotonated at N-1. We assume the presence of a hydrogen bond at N-1, which is modeled in the calculation by a water molecule (see "Discussion").

[c] This is the tryptophan cation radical, protonated at N-1 (Fig. 7*B*).

[d] This is the histidine neutral radical, deprotonated and hydrogen-bonded at both nitrogens. Side chain geometry is as shown in Fig. 8. Note the different numbering schemes for tryptophan and histidine. C-5 is not comparable in both radicals (Scheme 1). The cation radical is protonated at one nitrogen. Side chain geometry is as shown in Fig. 8. The experimental data do not agree with the spin densities calculated for a histidine neutral or cation radical. In particular, the large spin densities at C-2 (0.33) and C-5 (0.47) lead to very large and anisotropic hf-tensors from the ring protons (between 1.5 and 2.0 mT), which is not in agreement with the experimental values (see "Discussion").

[e] NA, not applicable. Position 4 in tryptophan is a non-magnetic ^{12}C atom (Scheme 1).

approach used here avoids this problem. Simulations of the 9.4 GHz EPR spectra yielded an hf-tensor data set that was used for simulations of the 94 GHz high-field EPR spectra, from which accurate g-tensors were obtained. This data set was further refined by simulations of both spectra with these g-tensor values, yielding finally a common hf- and g-tensor set (given in Table 1), which fits the EPR spectra at both frequencies equally well.

The obtained g-tensor values show very low anisotropy. Radicals with spin density on oxygen (like tyrosyls) have significantly larger g-tensor anisotropy, with typical values for tyrosyls of $g_{xx} = 2.0092$ to 2.0068 (depending on the environment polarity and hydrogen bonding), $g_{yy} \sim 2.0044$, and $g_{zz} \sim 2.0022$ (48, 51, 53, 61, 62). The g-tensor values obtained here for the radical in *P. eryngii* VP* are in perfect agreement with a tryptophan neutral radical, as reported for the Y122F variant of *E. coli* ribonucleotide reductase (34, 53, 62) and recently detected in VP from *B. adusta* (52). Theoretical g-tensor values (Table 1) were calculated with DFT for the tryptophan neutral radical, hydrogen-bonded at N-1 to a water molecule (Fig. 7), for two different side chain orientations. Considering a reported general $\sim 10\%$ overestimation by DFT

methods (63, 64) of the g-tensor shifts (Δg_{jj}) from the free electron value g_e, ($\Delta g_{jj} = g_{jj} - g_e$ ($jj = xx, yy, zz$), $g_e = 2.002319$), the calculated g-tensor values are in good agreement with the experimental values. Similar g-tensor values were, however, also calculated for the tryptophan cation radical (Table 2). Therefore, discrimination between a tryptophan neutral or cation radical is not possible based on the g-tensor values alone.

The common hf-tensor data set obtained from the 9.4 and 94 GHz EPR spectra shows the presence of two large rather isotropic proton hf-tensors typical for β-protons of the side chain, only two large anisotropic hf-tensors from two ring protons, and one large anisotropic hf-tensor from an $S = 1$ (^{14}N) hf-tensor (Table 1). From these data, experimental spin densities for C-3, for two other carbon ring positions, and for N-1 were deduced (Table 2, first column). Comparison with the calculated Mulliken spin densities for tryptophan and histidine neutral and cation radicals (Table 2) shows that such a spin density distribution is calculated only for the tryptophan neutral radical. According to the calculations, $\sim 60\%$ of the spin density is at C-3, followed by 23 and 18% at C-5 and C-7, giving rise to the observed ring proton hf-tensors; N-1 carries 26% spin density. This distribution is very similar to that

FIGURE 8. **Spin densities calculated with DFT (43), visualized using a contour value of 0.005 with the program MOLDEN (44).** *A*, histidine neutral radical, deprotonated and hydrogen-bonded to water molecules at both nitrogens (compare with Scheme 1). *B*, histidine cation radical, hydrogen-bonded at N-δ (N-4; see Scheme 1). Note that, for the neutral radical, both nitrogens show hydrogen bonds to a water molecule. *Blue*, positive spin densities; *red*, negative spin densities. For both radicals, large spin densities were calculated for C-3, giving rise to large hf-tensors of the side β-protons (Scheme 1), and for C-2. A particularly large spin density was calculated for the carbon between the two nitrogens (C-5; see Scheme 1), and only small and even negative spin densities were calculated for the two nitrogens. These values are not in agreement with the experimental values (see "Results"). The larger spin densities together with those from the tryptophan radicals are listed in Table 2.
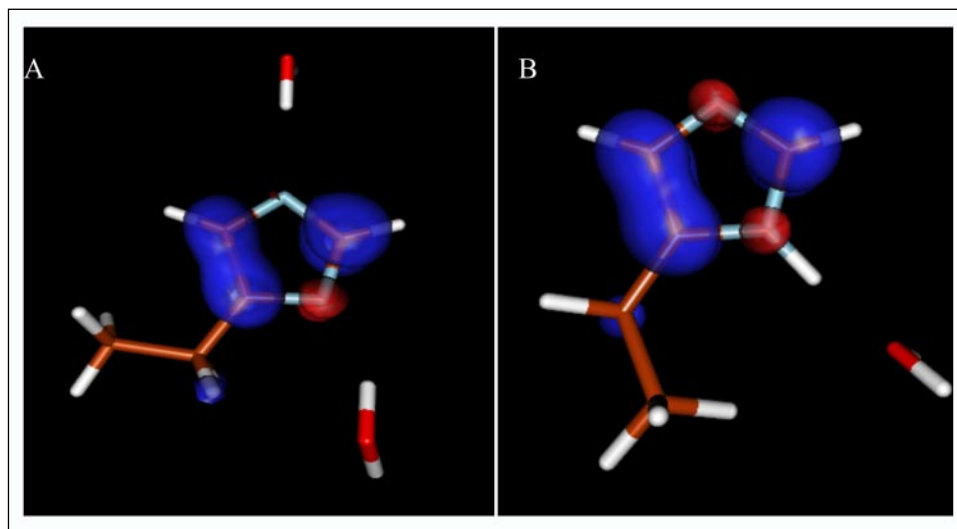
obtained previously for the tryptophan radical in the Y122F variant of *E. coli* ribonucleotide reductase (34). The calculations also predict small anisotropic hyperfine couplings for the proton at position 2 and for the water proton, hydrogen-bonded to N-1, in good agreement with the small proton hyperfine splitting observed in the pulse ENDOR spectra (Fig. 6 and Table 1). The tryptophan neutral radical presumably evolves from a short-lived cation radical that is generated from the proposed $Fe^{4+}=O$ porphyrin cation radical precursor by LRET, leaving the heme iron in the Fe^{4+} state, but promoting the cation radical state to the tryptophan. The tryptophan cation radical then, in a second step, becomes stabilized by deprotonation at N-1. This proton could be taken in by one of the oxygens of the nearby residue Glu[243] and then become hydrogen-bonded to the remaining lone electron pair of N-1 at the tryptophan. In any case, the second small anisotropic proton hf-tensor, observed by ENDOR, strongly supports a neutral radical hydrogen-bonded at N-1. The hf-tensor of this hydrogen-bonded proton is mostly of dipolar nature and is expected to be very similar for a hydrogen-bonded water proton or a proton from an amino acid residue as the hydrogen bond donor. For simplicity, the calculations were performed with water as the hydrogen bond donor, whereby the distance and geometry were obtained by energy minimization.

The calculations for the tryptophan cation radical predict significantly smaller spin densities for C-3 and N-1 and are not in agreement with the experimental results. In addition, a large positive spin density is predicted for C-2 and a large hf-tensor is expected for the NH proton (Fig. 7 and Table 2). The proton bound to the nitrogen and the proton at position 2 would both lead to additional large ring proton hf-tensors, giving rise to visible additional splitting in the EPR spectrum, which is clearly in contradiction with the experimental EPR spectra. In particular, the simulated 9.4 GHz EPR spectra were very sensitive to the multiplicity of the proton hyperfine couplings. Furthermore, the hf-tensor from a proton hydrogen-bonded to N-1, observed by ENDOR, is expected only in the case of the neutral radical. Hence, the obtained experimental set of g- and hf-tensor data and the deduced π-spin densities are in perfect agreement with a tryptophan neutral radical and do not support a tryptophan cation radical.

Because the possible involvement of a histidine radical has been discussed in some mechanistic studies (13, 65), we also performed calculations for the histidine neutral radical, deprotonated and hydrogen-bonded at both nitrogens, and for the cation radical, protonated at N-4 (Fig. 8 and Table 2). For the neutral radical, large spin densities were

calculated for C-2 and in particular for C-5. Significantly smaller spin density compared with the tryptophan neutral radical was calculated for C-3; and surprisingly, small and even negative spin densities were calculated for the two nitrogens. The calculated hf-tensor value for ring proton 5 (data not shown) was at least a factor of 2 larger than the values derived from the experimental spectra. On the other hand, the two calculated rather isotropic hf-tensor values of the side chain β-protons were significantly smaller than the experimental values, and the very small calculated ^{14}N hf-tensor elements were also in disagreement with the experimental EPR spectra. Interestingly, very similar spin densities were calculated for the histidine cation radical, with a proton bonded at N-4. The Mulliken spin densities and the calculated hf-tensor values for both forms of histidine radicals are clearly in disagreement with the experimental values. We therefore ruled out a histidine as site for the radical in *P. eryngii* VP.

Site-specific Assignment of the Radical to Trp[164]—It had been shown in previous studies (34, 53, 62) that the hf-tensor values of the side chain β-protons of a tryptophan neutral radical, like those of tyrosyl radicals (34, 61, 66), can vary significantly, even though the spin density at C-3 is very similar in all cases. The magnitude of the isotropic part (A_{iso}) of the hf-tensor of β-protons is a function of the spatial orientation of the side chain and is given by the McConnell relation (67) (Equation 3),

$$A_{iso}(\text{H-}\beta) = \rho_C^\pi (B' + B''\cos^2\theta) \qquad \text{(Eq. 3)}$$

where B' and B'' are empirical constants ($B' \sim 0$, $B'' = 5.0-5.8$ mT) and θ is the dihedral angle between the adjacent π-carbon p_z axis and the projected C-β–H-β bond (Scheme 1) (34, 51, 66). The dependence of $A_{iso}(\text{H-}\beta)$ from the side chain orientation with respect to the tryptophan indole plane is strong because $\cos^2\theta$ can vary between 1 and 0 for each of the two β-protons. Using the above range for the B'' value and considering tetragonal symmetry for the two side chain β-protons and the second side chain carbon (*i.e.* $\theta_1(\text{H-}\beta1) - \theta_2(\text{H-}\beta2) = 120°$) and a spin density of $\rho^\pi(\text{C-3}) \sim 0.52$ (1), dihedral angles of $\theta_1(\text{H-}\beta1) \sim \|15°\|$ and $\theta_2(\text{H-}\beta2) \sim \|45°\|$ (estimated error of $\pm5°$) were calculated from the isotropic part (A_{iso}) of the hf-tensors of the β-protons H-β1 and H-β2 given in Table 1. This side chain orientation for the tryptophan radical obtained from the experimental data is shown in Fig. 9 together with the orientations for the two VP residues Trp[164] and Trp[244] from the *P. eryngii* VP* crystal structure very recently solved at atomic resolution.

The side chain (R) orientation for Trp[244], taken from the x-ray struc-

FIGURE 9. **Locations and side chain orientations of tryptophan residues in *P. eryngii* VP.** *A*, distances from the two tryptophan residues (Trp^{164} and Trp^{244}) to heme in the VP* crystal structure determined at 1.33-Å resolution. *B* and *C*, orientations of C-β–H bonds and side chains (edge on view of the C-β–C-3 bond; see Scheme 1) for the VP* tryptophan radical obtained from the EPR data (*Exp.*) in comparison with Trp^{164} (*B*) and Trp^{244} (*C*) orientations in the VP* crystal structure. *R* corresponds to C-α.
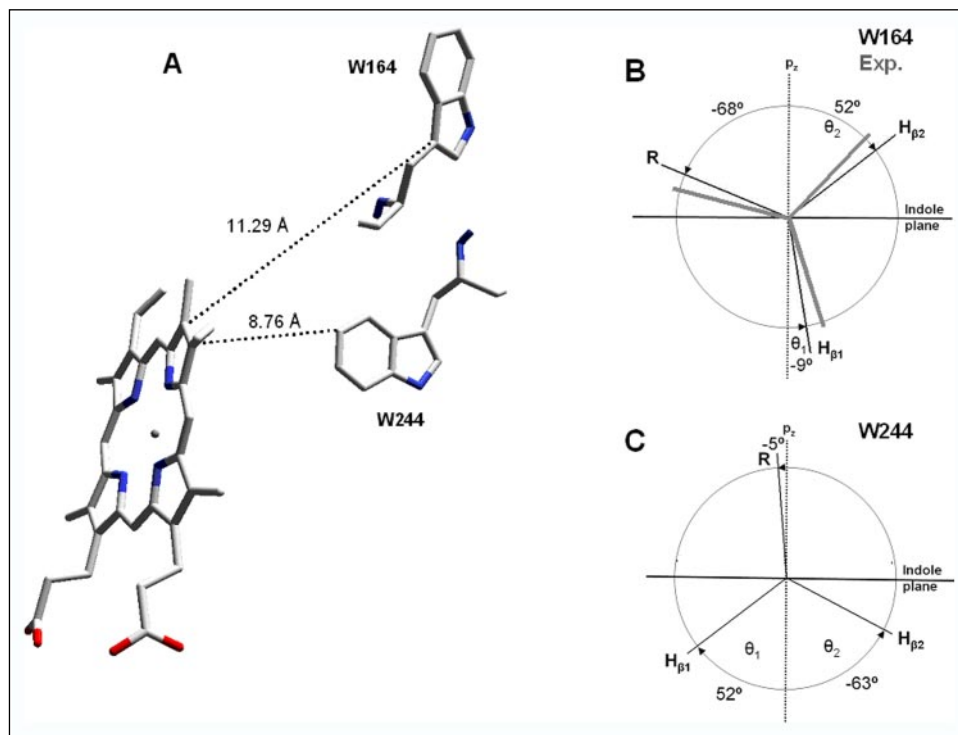
ture (Fig. 9*C*), is ~85° out of the indole plane. The dihedral angles for the β-protons are 52° for H-β1 and −63° for H-β2 and, for a tryptophan neutral radical, would lead to hf-tensor elements more than a factor of 2 smaller than those observed in the experiment (Table 1). However, for Trp^{164}, these β-proton dihedral angles are −9° and 52° (Fig. 9*B*), which is in fair agreement with the experimental range (15 ± 5° and 45 ± 5°) when considering that a small reorientation upon radical generation (68) could be possible (see above and Table 1). It is interesting to mention that these two tryptophan residues are homologous to Trp^{171} and Trp^{251} of *P. chrysosporium* LiP and have similar side chain orientations, although a third tryptophan residue (Trp^{17}) exists in LiP (whose side chain has the same orientation as LiP Trp^{251}) (26, 69). Based on the experimentally determined side chain geometry, we assign the tryptophan neutral radical in *P. eryngii* to Trp^{164}. Furthermore, kinetic data obtained with different single mutants (W164S and H232F) and one double mutant (W164S/P76H) have shown that the LRET pathway starting at Trp^{164} is the only pathway that is kinetically competent for the oxidation of (high redox potential) aromatic substrates by VP (70).

Closer inspection of the sequences of LiP from *P. chrysosporium* and VPL from *P. eryngii* shows that these enzymes have no tyrosines. In fact, the absence of tyrosine residues is a general characteristic of all ligninolytic peroxidases described up to the present (>30 available sequences) (15). This characteristic seems to be a strategy to prevent competitive generation of tyrosine radicals. In fact, charge transfer between tryptophan and tyrosine and its pH-dependent formation has been established (71) in dipeptides and in a cytochrome *c* peroxidase variant including a K^+-binding site (CcPK2) (72). It has been shown that the solution redox potential for the reaction of the tryptophan neutral radical (Trp $\rightleftharpoons$ Trp$^{\bullet}$ + H^+) is pH-dependent and is, at ambient pH values, higher than for the respective reaction of a tyrosine neutral radical. On the other hand, the potential required for generation of the cation radical (Trp $\rightleftharpoons$ Trp$^{\bullet+}$) is lower for tryptophan and very high for a tyrosine cation radical (73). However, these redox potentials are significantly influenced by the protein environment (72, 73). It is very possible that the true catalytic intermediate in VP is the tryptophan cation radical, which becomes (in

the absence of substrate), during the time needed for freezing, the protein deprotonated at the indole nitrogen to form the probably more stable observed tryptophan neutral radical. Formation of a relatively stable deprotonated neutral radical was also observed for a tryptophan radical generated by photoinduced electron transfer in azurin (54).

Moreover, the existence of exposed tyrosine residues may lead to enzyme inactivation due to intermolecular cross-linking (between the phenoxy radicals formed), as reported during spontaneous decay of cytochrome *c* peroxidase Compound I (74). Therefore, the absence of tyrosine residues in ligninolytic peroxidases could be a way of preventing enzyme inactivation by dimerization reactions.

Conclusion—Both forms of tryptophan radicals (neutral and cation) are observed in the electron transfer reaction of DNA photolyase (57, 75). Tryptophan cation radicals are observed for residues inside the protein, whereas the last radical in the chain, close to the surface of the protein, is deprotonated and becomes a neutral tryptophan (57). Similarly, we observed in *P. eryngii* a tryptophan neutral radical at position 164 (LiP Trp^{171}), which is located at the protein surface. Our results presented in this study strongly support mechanistic models that involve a tryptophan radical at this position (13, 28, 32). This tryptophan radical, generated close to the protein surface via LRET from a proposed $Fe^{4+}=O$ porphyrin π-cation radical precursor, provides a powerful reactant, which is apparently capable of oxidizing also large molecular mass substrates, which, because of their large size, are not able to reach the active heme site of VP. This ability makes the enzyme particular interesting for biological degradation of large molecules such as industrial dyes and lignin (9, 10).

Although our experimental data clearly show that a tryptophan neutral radical is formed in the course of the reaction of VP with H_2O_2, the detailed mechanism of the reaction still remains to be resolved (70). For instance, the actual catalytically active form of the radical in the presence of substrate could nevertheless alternatively be a tryptophan cation radical, which, in the absence of substrate, becomes deprotonated after ~10 s at the nitrogen to form the more stable neutral radical, which we observed. Additional experiments using fast freeze-quench techniques

with a time resolution of a few milliseconds, combined with EPR techniques, are envisaged to resolve earlier steps of the catalytic reaction of VP.

REFERENCES

1. Glenn, J. K., Morgan, M. A., Mayfield, M. B., Kuwahara, M., and Gold., M. H. (1983) *Biochem. Biophys. Res. Commun.* **114,** 1077–1083
2. Kuwahara, M., Glenn, J. K., Morgan, M. A., and Gold, M. H. (1984) *FEBS Lett.* **169,** 247–250
3. Tien, M., and Kirk, T. K. (1983) *Science* **221,** 661–663
4. Camarero, S., Böckle, B., Martínez, M. J., and Martínez, A. T. (1996) *Appl. Environ. Microbiol.* **62,** 1070–1072
5. Martínez, M. J., Ruiz-Dueñas, F. J., Guillen, F., and Martínez, A. T. (1996) *Eur. J. Biochem.* **237,** 424–432
6. Sarkar, S., Martínez, A. T., and Martínez, M. J. (1997) *Biochim. Biophys. Acta* **1339,** 23–30
7. Heinfling, A., Martínez, M. J., Martínez, A. T., Bergbauer, M., and Szewzyk, U. (1998) *FEMS Microbiol. Lett.* **165,** 43–50
8. Mester, T., and Field, J. A. (1998) *J. Biol. Chem.* **273,** 15412–15417
9. Heinfling, A., Ruiz-Dueñas, F. J., Martínez, M. J., Bergbauer, M., Szewzyk, U., and Martínez, A. T. (1998) *FEBS Lett.* **428,** 141–146
10. Heinfling, A., Martínez, M. J., Martínez, A. T., Bergbauer, M., and Szewyk, U. (1998) *Appl. Environ. Microbiol.* **64,** 2788–2793
11. Camarero, S., Ruiz-Dueñas, F. J., Sarkar, S., Martínez, M. J., and Martínez, A. T. (2000) *FEMS Microbiol. Lett.* **191,** 37–43
12. Ruiz-Dueñas, F. J., Martínez, M. J., and Martínez, A. T. (1999) *Mol. Microbiol.* **31,** 223–236
13. Ruiz-Dueñas, F. J., Camarero, S., Perez-Boada, M., Martínez, M. J., and Martínez, A. T. (2001) *Biochem. Soc. Trans.* **29,** 116–122
14. Pérez-Boada, M., Doyle, W. A., Ruiz-Dueñas, F. J., Martínez, M. J., Martínez, A. T., and Smith, A. T. (2002) *Enzyme Microb. Technol.* **30,** 518–524
15. Martínez, A. T. (2002) *Enzyme Microb. Technol.* **30,** 425–444
16. Dunford, H. B. (1999) *Heme Peroxidases*, Wiley-VCH, New York
17. Sivaraja, M., Goodin, D. B., Smith, M., and Hoffman, B. M. (1989) *Science* **245,** 738–740
18. Henriksen, A., Schuller, D. J., Meno, K., Welinder, K. G., Smith, A. T., and Gajhede, M. (1998) *Biochemistry* **37,** 8054–8060
19. Itakura, H., Oda, Y., and Fukuyama, K. (1997) *FEBS Lett.* **412,** 107–110
20. Pelletier, H., and Kraut, J. (1992) *Science* **258,** 1748–1755
21. Kishi, K., Kusters-van Someren, M., Mayfield, M. B., Sun, J., Loehr, T. M., and Gold, M. H. (1996) *Biochemistry* **35,** 8986–8994
22. Kusters-van Someren, M., Kishi, K., Lundell, T., and Gold, M. H. (1995) *Biochemistry* **34,** 10620–10627
23. Sundaramoorthy, M., Kishi, K., Gold, M. H., and Poulos, T. L. (1997) *J. Biol. Chem.* **272,** 17574–17580
24. Camarero, S., Sarkar, S., Ruiz-Dueñas, F. J., Martínez, M. J., and Martínez, A. T. (1999) *J. Biol. Chem.* **274,** 10324–10330
25. Banci, L., Camarero, S., Martínez, A. T., Martínez, M. J., Pérez-Boada, M., Pierattelli, R., and Ruiz-Dueñas, F. J. (2003) *J. Biol. Inorg. Chem.* **8,** 751–760
26. Poulos, T. L., Edwards, S. L., Wariishi, H., and Gold, M. H. (1993) *J. Biol. Chem.* **268,** 4429–4440
27. Schoemaker, H. E., Lundell, T. K., Floris, R., Glumoff, T., Winterhalter, K. H., and Piontek, K. (1994) *Bioorg. Med. Chem.* **2,** 509–519
28. Blodig, W., Doyle, W. A., Smith, A. T., Winterhalter, K., Choinowski, T. H., and Piontek, K. (1998) *Biochemistry* **37,** 8832–8838
29. Blodig, W., Smith, A. T., Doyle, W. A., and Piontek, K. (2001) *J. Mol. Biol.* **305,** 851–861
30. Choinowski, T., Blodig, W., Winterhalter, K., and Piontek, K. (1999) *J. Mol. Biol.* **286,** 809–827
31. Mester, T., Ambert-Balay, K., Ciofi-Baffoni, S., Banci, L., Jones, A. D., and Tien, M. (2001) *J. Biol. Chem.* **276,** 22985–22990
32. Blodig, W., Smith, A. T., Winterhalter, K., and Piontek, K. (1999) *Arch. Biochem. Biophys.* **370,** 86–92
33. Timofeevski, S. L., Nie, G., Reading, N. S., and Aust, S. D. (2000) *Arch. Biochem. Biophys.* **373,** 147–153
34. Lendzian, F., Sahlin, M., MacMillan, F., Bittl, R., Fiege, R., Pötsch, S., Sjöberg, B.-M.,
35. Gräslund, A., Lubitz, W., and Lassmann, G. (1996) *J. Am. Chem. Soc.* **118,** 8111–8120
35. Sahlin, M., Lassmann, G., Pötsch, S., Sjöberg, B.-M., and Gräslund, A. (1995) *J. Biol. Chem.* **270,** 12361–12372
36. Sambrook, J., and Russell, D. W. (2000) *Molecular Cloning: A Laboratory Manual,* 3rd Ed., Cold Spring Harbor Press, Cold Spring Harbor, NY
37. Brudvig, G. W. (1995) *Methods Enzymol.* **246,** 536–554
38. Beinert, H., and Orme-Johnson, W. H. (1967) in *Magnetic Resonance in Biological Systems* (Ehrenberg, A., Malmstrom, B. J., and Vanngard, T., eds) pp. 221–247, Pergamon Press, Oxford
39. Rupp, H., Rao, K. K., Hall, D. O., and Cammack, R. (1978) *Biochim. Biophys. Acta* **537,** 255–260
40. Stesmans, A., and van Gorp, G. (1989) *Rev. Sci. Instrum.* **60,** 2949–2952
41. Rieger, P. H. (1982) *J. Magn. Reson.* **50,** 485–489
42. Mombourquette, H. J., and Weil, J. E. (1992) *J. Magn. Reson.* **99,** 37–44
43. Frisch, M. J., Trucks, G. W., Schlegel, H. B., Scuseria, G. E., Robb, M. A., Cheeseman, J. R., Montgomery, J. A., Jr., Vreven, T., Kudin, K. N., and Burant, J. C., (2003) *Gaussian 03, Revision B.04*, Gaussian, Inc., Pittsburgh, PA
44. Schaftenaar, G., and Noordik, J. H. (2003) *J. Comput. Aided Mol. Des.* **14,** 123–134
45. Smulevich, G. (1998) *Biospectroscopy* **4,** S3–S17
46. Marquez, L., Wariishi, H., Dunford, H. B., and Gold, M. H. (1988) *J. Biol. Chem.* **263,** 10549–10552
47. Renganathan, V., and Gold, M. H. (1986) *Biochemistry* **25,** 1626–1631
48. Ivancich, A., Jakopitsch, C., Auer, M., Un, S., and Obinger, C. (2003) *J. Am. Chem. Soc.* **125,** 14093–14102
49. Ivancich, A., Mazza, G., and Desbois, A. (2001) *Biochemistry* **40,** 6860–6866
50. Villegas, J. A., Mauk, A. G., and Vazquez-Duhalt, R. (2000) *Chem. Biol.* **7,** 237–244
51. Schünemann, V., Lendzian, F., Jung, C., Contzen, J., Barra, A. L., Sligar, S. G., and Trautwein, A. X. (2004) *J. Biol. Chem.* **279,** 10919–10930
52. Pogni, R., Baratto, M. C., Giansanti, S., Teutloff, C., Verdin, J., Valderrama, B., Lendzian, F., Lubitz, W., Vazquez-Duhalt, R., and Basosi, R. (2005) *Biochemistry* **44,** 4267–4274
53. Bleifuss, G., Kolberg, M., Pötsch, S., Hofbauer, W., Bittl, R., Lubitz, W., Gräslund, A., Lassmann, G., and Lendzian, F. (2001) *Biochemistry* **40,** 1562–1568
54. Miller, J. E., Gradinaru, C., Crane, B. R., Di Bilio, A. J., Wehbi, W. A., Un, S., Winkler, J. R., and Gray, H. B. (2003) *J. Am. Chem. Soc.* **125,** 14220–14222
55. Lubitz, W., and Lendzian, F. (1996) in *Advances in Photosynthesis: Biophysical Techniques in Photosynthesis* (Amesz, J., and Hoff, A. J., eds) Vol. 3, pp. 255–275, Kluwer Academic Publishers, Dordrecht, The Netherlands
56. Schweiger, A. (1991) *Angew. Chem. Int. Ed. Engl.* **30,** 265–292
57. Aubert, C., Vos, M. H., Mathis, P., Eker, A. P., and Brettel, K. (2000) *Nature* **405,** 586–590
58. O'Malley, P. J., and Ellson, D. A. (1996) *Chem. Phys. Lett.* **260,** 492–498
59. Wertz, J. E., and Bolton, J. R. (1986) *Electron Spin Resonance: Elementary Theory and Practical Application*s, Chapman & Hall, New York
60. Bender, C. J., Sahlin, M., Babcock, G. T., Barry, B. A., Chan-Drashekar, T. K., Salowe, S. P., Stubbe, J., Lindström, B., Peterson, L., Ehrenberg, A., and Sjöberg, B.-M. (1989) *J. Am. Chem. So*c. **111,** 8076–8083
61. Un, S., Gerez, C., Elleingand, E., and Fontecave, M. (2001) *J. Am. Chem. Soc.* **123,** 3048–3054
62. Lendzian, F. (2005) *Biochim. Biophys. Acta* **1707,** 67–90
63. Engström, M., Himo, F., Gräslund, A., Minaev, B., Vahtras, O., and Agren, H. (2000) *J. Phys. Chem. A* **104,** 5149–5153
64. Kaupp, M., Gress, T., Reviakine, R., Malkina, O. L., and Malkin, V. G. (2003) *J. Phys. Chem. B* **107,** 331–337
65. Johjima, T., Itoh, N., Tokimura, F., Nakagawa, T., Wariishi, H., and Tanaka, H. (1999) *Proc. Natl. Acad. Sci. U. S. A.* **96,** 1989–1994
66. Himo, F., Gräslund, A., and Eriksson, L. A. (1997) *Biophys. J.* **72,** 1556–1567
67. Edmonds, D. T., and Summers, C. P. (1973) *J. Magn. Reson.* **12,** 134–142
68. Högbom, M., Galander, M., Andersson, M., Kolberg, M., Hofbauer, W., Lassmann, G., Nordlund, P., and Lendzian, F. **(**2003) *Proc. Natl. Acad. Sci. U. S. A.* **100,** 3209–3214
69. Piontek, K., Glumoff, T., and Winterhalter, K. (1993) *FEBS Lett.* **315,** 119–124
70. Pérez-Boada, M., Ruiz-Dueñas, F. J., Pogni, R., Basosi, R., Choinowski, T., Martínez, M. J., Piontek, K., and Martínez, A. T. (2005) *J. Mol. Biol.* **354,** 385–402
71. Reece, S. Y., Stubbe, J., and Nocera, D. G. (2005) *Biochim. Biophys. Acta* **1706,** 232–238
72. Barrows, T. P., Bhaskar, B., and Poulos, T. L. (2004) *Biochemistry* **43,** 8826–8834
73. Tommos, C., Skalicky, J. J., Pilloud, D. L., Wand, A. J., and Dutton, P. L. (1999) *Biochemistry* **38,** 9495–9507
74. Spangler, B. D., and Erman, J. E. (1986) *Biochim. Biophys. Acta* **872,** 155–157
75. Stubbe, J., Nocera, D. G., Yee, C. S., and Chang, M. C. (2003) *Chem. Rev.* **103,** 2167–2201